01 Feb 2023

Selection of Solidification Pathway in Rapid Solidification Processes

Nima Najafizadeh

Men G. Chu

Yijia Gu
Missouri University of Science and Technology, guyij@mst.edu

Recommended Citation

N. Najafizadeh et al., "Selection of Solidification Pathway in Rapid Solidification Processes," *Physical Review Materials*, vol. 7, no. 2, article no. 023403, American Physical Society, Feb 2023.
The definitive version is available at https://doi.org/10.1103/PhysRevMaterials.7.023403

Selection of solidification pathway in rapid solidification processes

Nima Najafizadeh,[1] Men G. Chu,[2] and Yijia Gu[1,*]
[1]Department of Materials Science and Engineering, Missouri University of Science and Technology, Rolla, Missouri 65409, USA
[2]Chu Metallurgical Consulting, Export, Pennsylvania 15632, USA

(Received 29 November 2022; accepted 23 January 2023; published 21 February 2023)

Rapid solidification processing of alloys enables the formation of exotic nonequilibrium microstructures. However, the interrelationship between the processing parameters and the resulting microstructure is yet to be fully understood. In melt spinning (MS) and additive manufacturing (AM) of rapidly solidified alloys, opposite microstructure development sequences were observed. A fine-to-coarse microstructural transition is typically observed in melt-spun ribbons, whereas melt pools in AM exhibit a coarse-to-fine transition. In this paper, the microstructural evolutions during these two processes are investigated using phase-field modeling. The variation of all key variables of the solid-liquid interface (temperature, composition, and velocity) throughout the entire rapid solidification of AM and MS processes was acquired with high accuracy. It is found that the onset of nucleation determines the selection of the solidification pathway and, consequently, the evolution of temperature and velocity of the interface during the rapid solidification. The switching of control mechanisms of the solid-liquid interface, which happens in both processes but in opposite directions, is found to cause the velocity jump and disrupt the microstructure development.

DOI: 10.1103/PhysRevMaterials.7.023403

I. INTRODUCTION

The rapid solidification technique was developed on the foundation of the early works from Duwez *et al.* [1] and Clement *et al.* [2] on quenching the silver-copper alloys at high enough cooling rates to suppress the usual nucleation and growth of the equilibrium phases. In essence, rapid solidification can be achieved when the following conditions are met: (1) high undercooling before the onset of solidification, (2) high velocity of solidification front, and (3) high cooling rate during the solidification process [3]. In return, it offers majorly three benefits: extended solid solubility, refined structures, and the formation of exotic nonequilibrium phases.

Despite noteworthy attempts for microstructure mapping based on the processing variables [4–8], some of the diverse microstructures formed in rapid solidification processes still cannot be well explained. For example, additive manufacturing (AM) and melt spinning (MS), two well-known examples of the rapid solidification process, can form different inhomogeneous microstructures. In many additively manufactured alloys, various layered microstructures are observed in the melt pools. Depending on alloy chemistries and processing variables, the individual layer may be filled with primary intermetallic particles [9], eutectic structures [10], cellular/dendritic structures [11], or superfine equiaxed grains [12–18]. As seen in an Al-2.5Fe sample [19] shown in Fig. 1(a), along the growth direction, the first layer (next to the melt pool boundary) exhibits coarser microstructural features and transforms to a finer microstructure in the next layer (toward the melt pool center). Melt-spun ribbons typically exhibit an inhomogeneous microstructure, with a very fine microcellular layer that abruptly transforms into a coarser cellular or dendritic structure. The fine microcellular structure was used to be described as "featureless" because it did not display any observable optical features [20]. In contrast to AM, the microstructural transition in MS [21] goes from fine to coarse, as shown in Fig. 1(b). The opposite microstructure transition sequence indicates that the solidification pathways are different in these two processes, although their cooling rates (10^5–10^7 K/s) are similar. In addition, the clear boundaries of layered microstructures in both AM and MS suggest that, when the solid-liquid interface advances to those locations, a sharp transition in a controlling variable leads to an immediate change of microstructure. Thus, it makes sense to inquire as to what variable is in control. What causes this variable to change abruptly? Why do two rapid solidification processes that have similar cooling rates have opposing microstructure formation sequences? Those queries are still unaddressed, though.

The microstructure development of rapidly solidified alloys is controlled by the interplay between interfacial velocity, temperature, and solute concentration at the solid-liquid interface [23]. Due to the large interfacial velocity, the solidification may not have enough time to reach the local thermodynamic equilibrium state. The ergodicity is broken. Therefore, the interface dynamics (or how the interface variables evolve) of rapid solidification is complicated. As shown in Fig. 1(c), the morphology (solidification mode) is determined by the temperature gradient in the liquid and the interface velocity [22]. The temperature and solute concentration

*yijia.gu@mst.edu

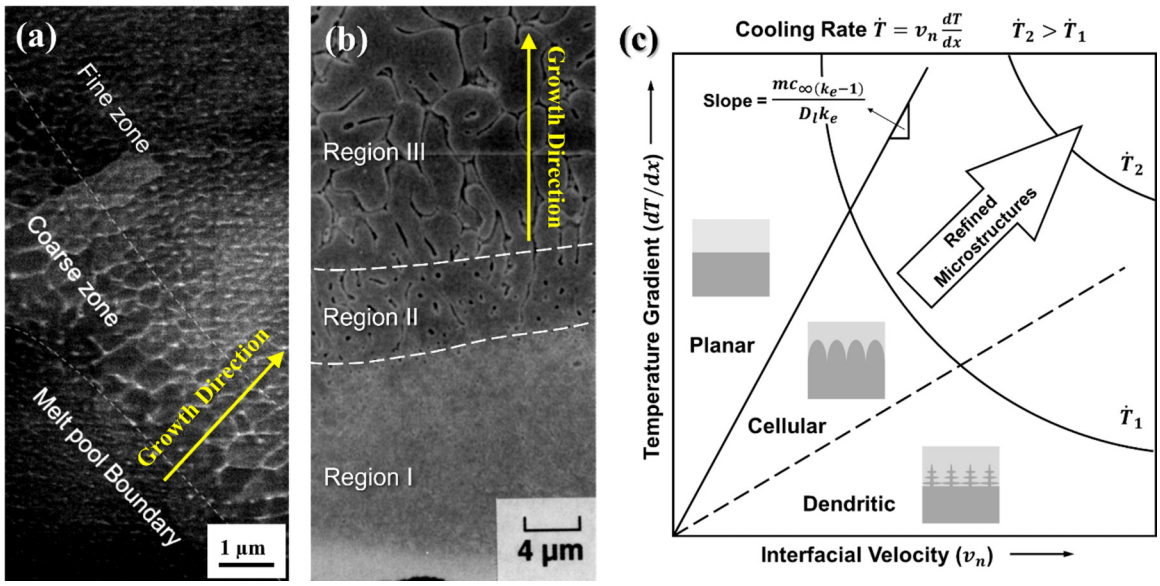

FIG. 1. (a) Scanning electron microscopy (SEM) image showing the microstructure of Al-2.5Fe processed by additive manufacturing (reproduced with permission from Ref. [19]). (b) SEM image showing the microstructure of Al-2Fe processed by melt spinning (reproduced with permission from Ref. [21]). (c) Modes of solidification as a function of temperature gradient in the liquid ($\partial T/\partial x$) and interfacial velocity (v_n) [22].

at the solid-liquid interface cannot be directly measured due to the spatial and temporal resolution limit of current characterization techniques. Although the interface velocity v_n can be experimentally assessed using *in situ* x-ray imaging [24] or dynamic transmission electron microscopy [25–28], both methods are very challenging. Due to those experimental challenges and limitations, theoretical studies play a vital role in the research of rapid solidification processes.

There exist a few analytical models on rapid solidification [29–35]. They can be used to construct the microstructure selection maps (MSMs) for rapid solidification, which predict the microstructure for a given combination of composition and interface velocity [23,32,36]. However, the interface velocity needs to be known *a priori* to predict the microstructure when using MSMs. The interface velocity may change dramatically during the solidification of a melt pool or a melt-spun ribbon. Accordingly, a microscopic model that couples the thermal diffusion with the liquid-to-solid phase transformation during the rapid solidification is needed to correctly predict the temperature evolution at the interface. The most feasible physics-based candidate to build such a model is the so-called phase-field method [37–39], which avoids solving the notorious moving boundary problem (the so-called Stefan problem) associated with the phase transition. Several phase-field models have been developed specifically to study rapid solidification [40–52]. Nevertheless, most of the current phase-field studies of rapid solidification processes only considered solute diffusion and neglected thermal diffusion by imposing a predefined temperature profile. Those treatments may be able to reproduce a uniform microstructure for certain locations, but they are inadequate to simulate the development of those inhomogeneous microstructures due to the negligence of complex thermal history during the entire solidification of the whole melt pool or melt-spun ribbon.

In this paper, a phase-field model for dilute binary alloys is adopted to explore the microstructure development in those rapid solidification processes. This model considers the coupled thermal-solute diffusion and solute trapping, enabling direct access to the evolution of the key variables (velocity, temperature, and solute concentration) at the interface throughout the entire rapid solidification process. The development of those microstructures observed in AM and MS will be correlated to the variations of those interfacial variables from phase-field simulations, and the formation mechanism will be revealed. Specifically, the nucleation or the onset of the solidification of AM and MS will be explored. The resulting solidification pathway and the development of inhomogeneous microstructures will be elucidated. The transition from one microstructure to the other will be explained using the proposed theory of control mechanism switching for both AM and MS. The formation of the fine microcellular region in MS and the effect of nucleation and alloy composition will be discussed in detail. The paper will conclude with a summary of the key findings and a perspective on how those findings may facilitate future research in rapid solidification processes.

II. METHODOLOGY

A. Phase-field model

In this paper, we employed a phase-field model with solute trapping and coupled thermal-solute diffusion for a dilute binary alloy system to investigate the microstructure development during the rapid solidification of fusion-based metal AM and MS processes. The kinetic equations that govern the evolution of phases (ϕ), composition (c), and temperature (T) include

$$\tau \frac{\partial \phi}{\partial t} = W^2 \nabla^2 \phi + \phi - \phi^3 - \lambda(\theta + Mc_\infty U)(1-\phi^2)^2, \quad (1)$$

$$\frac{1+k-(1-k)\phi}{2}\left(\frac{\partial U}{\partial t}\right)=\nabla\left(D_l\frac{1-\phi}{2}\nabla U+J_{\text{at}}\right)+\frac{1+(1-k)U}{2}\left(\frac{\partial \phi}{\partial t}\right), \quad (2)$$

$$\frac{\partial \theta}{\partial t}=\alpha\nabla^2\theta+\frac{1}{2}\frac{\partial \phi}{\partial t}, \quad (3)$$

where ϕ is the order parameter denoting solid ($\phi=1$) and liquid ($\phi=-1$) phases, $\tau=\frac{1}{HM_\phi}$ is the interface attachment time scale, H is the barrier height of the double-well potential, M_ϕ is the phase-field mobility related to the kinetics of interface, t is time, W is a measure of solid-liquid interface width, λ is a dimensionless coupling constant, $\theta=\frac{T-T_m-mc_\infty}{L/c_p}$ is the normalized undercooling, T_m is the melting temperature of the alloy, L is the generated latent heat, c_p is the specific heat capacity at constant pressure, $M=-\frac{m(1-k)}{L/c_p}$ is the scaled slope of the liquidus line (m), c_∞ is the initial concentration of the alloy, $U=\frac{1}{1-k}[\frac{2c/c_\infty}{1+k-(1-k)\phi}-1]$ is the normalized solute concentration, k is the partition coefficient, D_l is the diffusivity of the solid in the liquid, J_{at} is the antitrapping current term [53], and α denotes the thermal diffusivity which is assumed to be equal for the solid and liquid phases. The solute trapping effect is considered by modifying J_{at} following the approach of Pinomaa and Provatas [45]. A detailed description of the model along with the numerical testing and validation can be found in Ref. [54] and its supplemental material.

The focus of this paper is to comprehend the fundamental physics of the moving solid-liquid interface and how it affects the formation of different microstructures during the rapid solidification of the melt pool and melt-spun ribbon in AM and MS, respectively. Therefore, the overall simulation size must be large enough to cover the entire melt pool or ribbon thickness and account for the superfast thermal diffusion. Meanwhile, the grid size should be small enough to appropriately capture the dynamics of the interface at which partitioning of solute, dissipation of latent heat, and variation of interfacial velocity occur. (It should be noted that the Kim-Kim-Suzuki model [55], which is typically used to arbitrarily increase the grid size for large simulations, does not apply to this paper because the interface is not at equilibrium.) These two requirements lead to a simulation size of at least 40 000 grid points in one dimension (1D) with a grid size of ~ 1.4 nm (for a melt pool of 50 μm). The simulation size is simply squared for a two-dimensional (2D) case, which makes it extremely challenging due to considerable computational cost. We chose to perform 1D simulations of the entire melt pool or melt-spun ribbon to capture the evolution of temperature during the entire solidification process while sacrificing the curvature effect. Hence, our phase-field model cannot provide direct 2D or 3D morphology information for dendritic or cellular structures. However, the contribution of curvature undercooling to overall undercooling becomes minimal as the amount of undercooling exceeds the freezing range or when the undercooling is significantly small [35]. The solid-liquid interface in the 1D model is the interface on the primary dendrite tip (for dendritic growth) or cell tip (for cellular growth), which corresponds to the growth front or solidification front. The simulated interface velocity can be directly compared with measured growth rate by *in situ* x-ray imaging [24] or dynamic transmission electron microscopy [56,57]. In addition, the simulated evolution of the growth front, including the temperature, velocity, and solute concentration, also determines the formation of primary solid phase, which makes up the skeleton of the solidification microstructure. Therefore, the 1D configuration will not only minimize the computational costs but will also maintain the generality of the results by capturing the evolution of the dominant variables at the fast-moving interface and predicting the resulting microstructures.

B. Simulation setup

As a result of a complex series of physical interactions between the laser beam and the irradiated material in fusion-based AM, the geometry of the molten metal can be considered as a channel formed by connecting many repeating hemispherical melt pools along the traveling direction of the heat source. Therefore, a hemispherical melt pool can be regarded as the representative unit for the entire AM process. It is presumable that the melt-pool shape will remain constant under the quasi-steady-state processing conditions used in this analysis. Consequently, the solidified melt pools resulted from each laser path will make up the final microstructure. In MS, the melt-spun ribbon will form bottom to top with a rectangular cross-section. The repeatability of the solidified microstructure across the length of the ribbon will make the rectangular cross-section a representative of the melt-spun ribbon. Accordingly, the MS and AM simulations were performed in a Cartesian and spherical coordinate system, respectively. As depicted in Figs. 2(a) and 2(b), the hemispherical geometry assumed for the melt pool in AM makes the spherical coordinate a good fit for solving the phase-field equations in 1D; meanwhile, the Cartesian coordinate is more suited for MS since the ribbon surface is parallel to the substrate copper wheel. Both the order parameter (ϕ) and normalized solute concentration (U) were subjected to no-flux boundary conditions in all phase-field simulations. For thermal evolution, two separate sets of boundary conditions were adopted based on the most realistic scenarios for the two examined rapid solidification processes in this paper. A no-flux boundary condition was applied to the melt pool center, while a fixed-flux boundary condition was applied to the outer surface of the hemisphere to establish a constant cooling rate ($\dot{T}=10^7$ K/s) at the melt pool boundary [Fig. 2(a)]. In the case of MS simulations, a no-flux boundary condition was used at the free surface of the ribbon, whereas on the chill side where a small solid nucleant was initially introduced, an interfacial heat conduction boundary condition was implemented [Fig. 2(b)]. The interfacial heat conduction boundary condition is written as [58,59]

$$-K\frac{\partial T}{\partial x}=-h(T-T_\infty), \quad (4)$$

where $K=200\,\text{W m}^{-1}\,\text{K}^{-1}$ is the thermal conductivity, $h=0.75\times10^6\,\text{W m}^{-2}\,\text{K}^{-1}$ denotes the heat transfer coefficient, and $T_\infty=300$ K is the constant temperature of the rotating wheel.

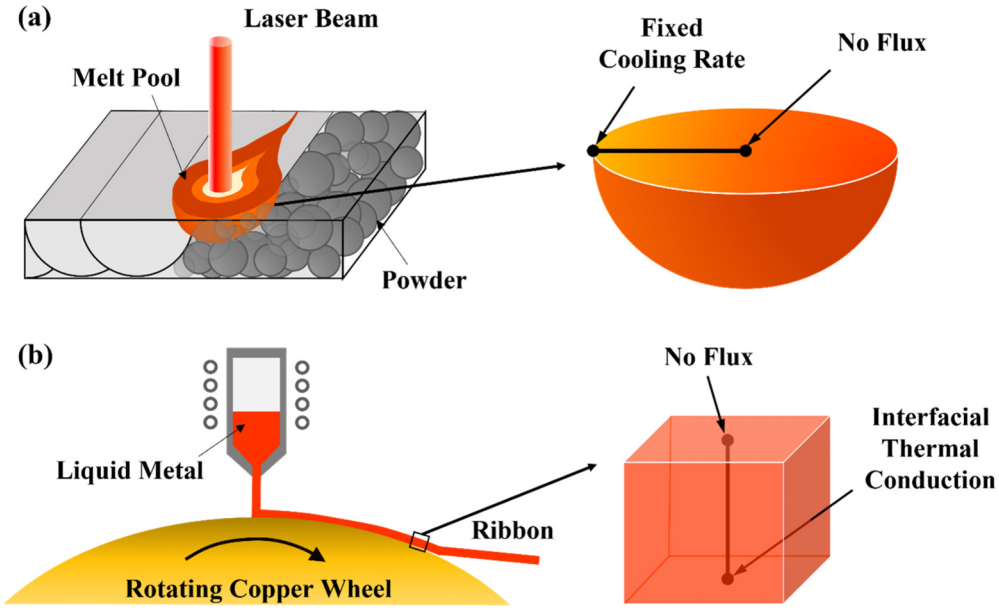

FIG. 2. Schematics of geometry and assumed boundary conditions for melt spinning (MS) and additive manufacturing (AM) processes: (a) layer-by-layer geometry of AM and thermal boundary conditions of hemispherical melt pool, and (b) MS setup and thermal boundary conditions of melt-spun ribbon.

Al-2 wt. % Fe (hereinafter referred to as Al-2Fe) is chosen as the subject material in this paper since experimental studies for both AM and MS processes were available for validating our findings. In our simulations, almost all the material properties are from either experimental measurement [60] or fitted from the equilibrium Al-Fe binary phase diagram. Table I provides a comprehensive list of all the parameters utilized in the phase-field model. It is noteworthy that the value of phase-field mobility M_ϕ is chosen to match the observed interface velocity in the rapid solidification of aluminum alloys since it is related to the interface velocity and can only be determined by matching the experimental observation. In addition, the solute trapping velocity of the phase-field model (V_D^{PF}) was determined following the approach of Pinomaa and Provatas [45].

TABLE I. Phase-field model parameters of Al-2Fe.

Latent heat of fusion L	9.47×10^8 J m^{-3} [60]
Specific heat capacity c_p	2.81×10^6 J K^{-1} m^{-1} [60]
Interfacial energy γ	0.158 J m^{-2} [61]
Melting temperature T_m	933.47 K[a]
Solute diffusivity in liquid D_l	4×10^{-9} m^2 s^{-1}
Thermal diffusivity α	4×10^{-5} m^2 s^{-1}
Initial alloy concentration c_∞	2 wt.%
Equilibrium partition coefficient k	0.025[a]
Slope of liquidus line m	-3.48 K(wt. %)$^{-1}$[a]
Computational interface width W_0	1.76×10^{-9} m
Mesh spacing dx	0.8 W
Time spacing dt	0.01 τ
Solute trapping velocity V_D^{PF}	0.75 m s^{-1}[b]
Solute trapping parameter A	3.01[b]
Phase-field mobility M_ϕ	7 m^3 J^{-1} s^{-1}
Interface width	5 nm

[a]Fitted to the phase diagram generated by Thermo − Calc™ using TCAL database.
[b]Achieved by fitting to the continuous growth model following the approach of Pinomaa and Provatas [45].

Both simulations were started with a homogeneous liquid at a temperature slightly above the liquidus (940 K), but the rapid solidification of AM and MS was configured differently to reflect their distinctions in the nucleation of the solid phase. In the case of AM, a small solid nucleus was introduced on one side of the domain (melt pool boundary) from the beginning, which grew into the liquid as the simulation progressed. This setup was to mimic the epitaxial growth from the previous layer observed in most AM microstructures, as almost no driving force is required for this type of nucleation. In MS simulations, the nucleation requires a much higher driving force, as the substrate (Cu) is a material with quite different lattice parameters. Consequently, the solid phase was not introduced until the temperature at the chill side dropped below a predefined critical temperature to ensure enough undercooling is provided for the nucleation in MS. For this paper, the undercooling ranging from 233 to 373 K was investigated. The corresponding nucleant size can be calculated using the free growth model [61]. The analysis of nucleation and undercooling selection is detailed in the Supplemental Material [62].

III. RESULTS AND DISCUSSION

A. Selection of solidification pathway

The solidification paths in AM and MS can be discussed in relation to the opposite microstructure transition sequences commonly observed in these two processes. For this purpose, the variation of interfacial temperature during the solidification of AM and MS processes as a function of both solid-liquid interface position and time are plotted in

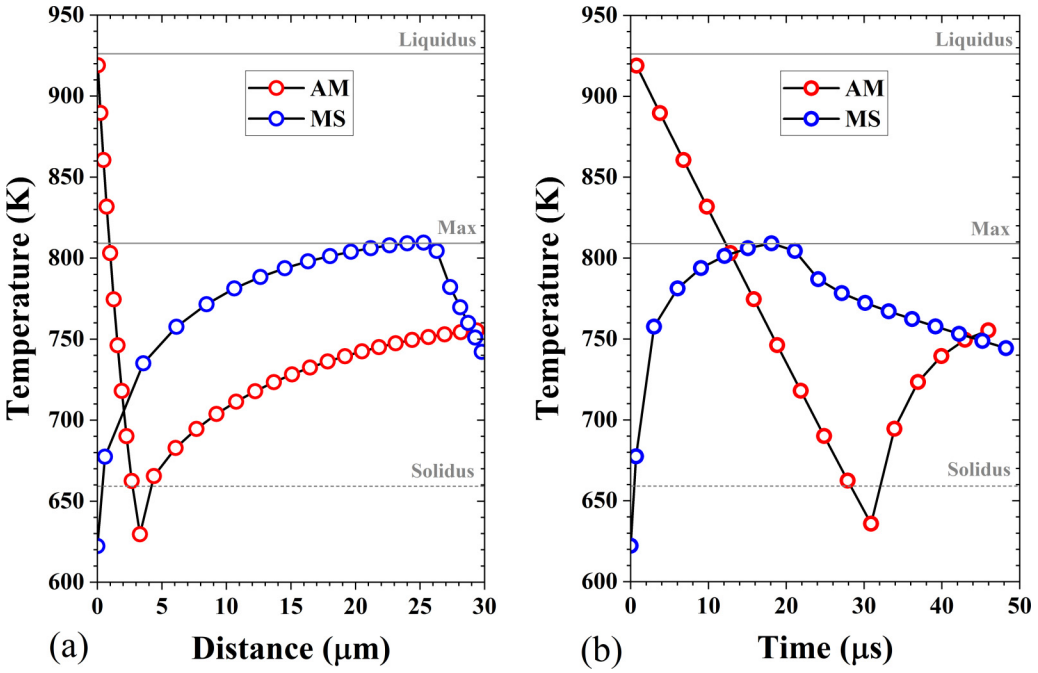

FIG. 3. The evolution of the interfacial temperature throughout the solidification process in additive manufacturing (AM) and melt spinning (MS): (a) temperature vs interface position, and (b) temperature vs time.

Figs. 3(a) and 3(b), respectively. An undercooling of 311 K was applied before the onset of solidification in MS, and the liquidus and solidus were obtained at the alloy composition (Al-2 wt. % Fe). Despite having a comparable cooling rate, the solidification paths taken by AM and MS are clearly differentiable, as they start solidifying at quite different temperatures and proceed in opposite directions. As the solidification in AM begins below the liquidus line, the temperature starts decreasing until it falls below the solidus line at a distance of ∼3 μm from the melt pool boundary, after which it continually rises. In the case of MS, the molten alloy starts solidifying at a temperature well below the solidus. The temperature then gradually rises until it ultimately reaches its maximum at ∼25 μm away from the chill side, at which point it starts to decline.

The AM and MS temperature profiles show distinct alterations at certain times and locations within the time and space domains. Accordingly, we speculate that those alternations correspond to the microstructural transitions commonly observed in these two processes. To further explore this idea, the relevant interfacial velocity fluctuations at the alternation points will be examined in the next subsection.

B. Selection of microstructures

Figure 4 depicts the interfacial growth velocity vs solid-liquid interface position for MS and AM simulations. Both velocity profiles consist of a high- and a low-velocity regime; however, the order of these velocity stages is reversed. The solidification starts at zero velocity in the AM simulation and steadily increases within the first few micrometers from the melt pool boundary. Then the growth velocity abruptly accelerates and enters the high-velocity regime followed by a plateau with a minor reduction for the rest of the melt pool length. The sharp interface velocity change is caused by the switching of the control mechanisms, i.e., from solute diffusion- to thermal diffusion-controlled growth [63]. Similar growth velocity change was observed during the

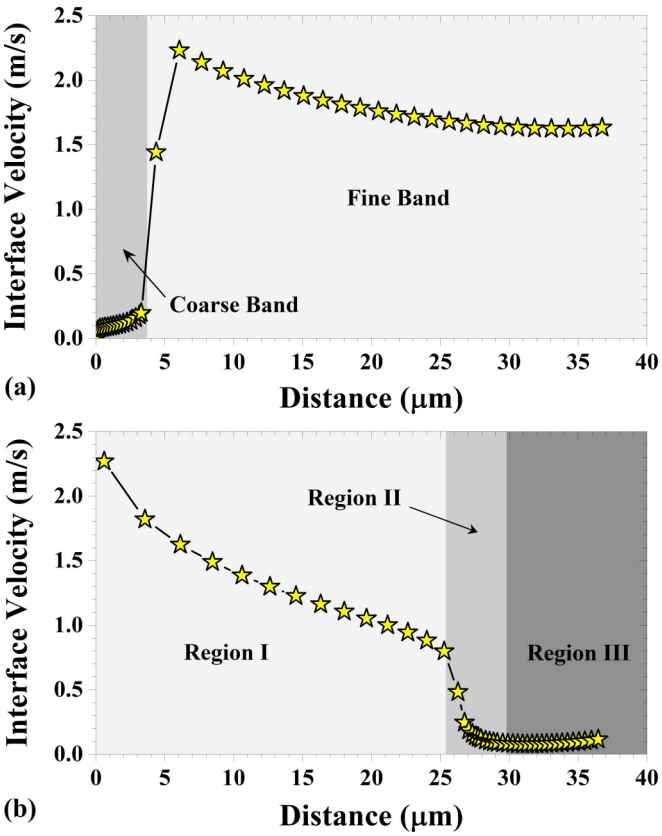

FIG. 4. Interface velocity as a function of the distance from the boundaries of the solidified microstructure for Al-2Fe in (a) additive manufacturing (AM), and (b) melt spinning (MS).

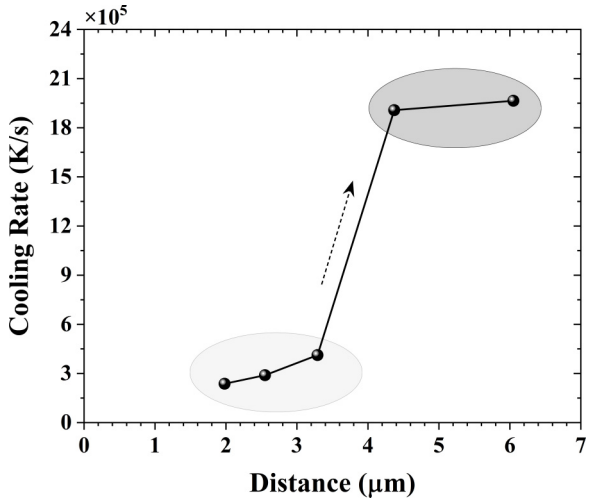

FIG. 5. The change in cooling rate with respect to distance from the melt pool boundary.

resolidification of a melt pool in Ti6Al4V using *in situ* x-ray imaging [24]. Since the size of the solidified microstructure features is strongly affected by the interface velocity, a sudden refining of microstructures is expected to occur at ∼3 μm away from the melt pool boundary, where the velocity jump took place. To quantify this microstructural variation, we calculated the cooling rates ($\dot{T} = v_n \cdot dT/dx$) before and after the velocity jump and plotted them in Fig. 5. As depicted in Fig. 1(c), the microstructure constituents will decrease in size as the cooling rate rises. The quantitative relationship between dendrite arm spacing λ (or cell size for cellular structures) and the cooling rate $\dot{T}$ is found as

$$\lambda = a\,\dot{T}^n, \tag{5}$$

where a is a material constant, and n ranges from $-\frac{1}{2}$ to $-\frac{1}{3}$ for metals and alloys [64,65]. As shown in Fig. 5, a cooling rate change from 0.25×10^6 to 2.1×10^6 K/m was observed before and after the velocity jump (at ∼3 μm away from the melt pool boundary). Correspondingly, a dendrite arm spacing/cell size change of 2–3 times is expected using the relationship above. The simulation results are consistent with experimentally observed morphology change. Qi *et al.* [19] studied the laser powder bed fusion of near-eutectic Al-Fe binary alloys. As shown in their scanning electron microscopy (SEM) image of the as-built Al-2.5Fe alloy [Fig. 1(a)], a band of relatively coarse cellular microstructure forms first near the melt pool boundaries. The coarse cellular band is replaced by a much finer cellular microstructure after ∼2 μm from the melt pool boundary, and the cell size change is ∼2–3 times. Those observed microstructure features agree quantitatively with the phase-field predictions.

Conversely, the MS simulation for Al-2Fe suggests a different sequence of microstructure development. The solidification starts at its maximum velocity in the melt-spun ribbon, then gradually decreases until it reaches a transition point ∼25 μm away from the chill side. After that, the velocity abruptly decreases and enters the low-velocity regime. The transition between high- and low-velocity regimes takes place over a relatively short portion of the solidified ribbon microstructure with a thickness of ∼3 μm. Eventually, the velocity profile settles into the low-velocity regime and remains almost unchanged. This velocity transition indicates that a fine-to-coarse morphology change exists within the developed microstructure. Our simulation results are at least semiquantitatively consistent with experimental observations of the Al-2Fe melt-spun ribbon reported by Chu and Granger [21]. They identified the existence of a three-region microstructure with distinguishable microstructural features. As shown in Fig. 1(b), starting from the bottom side of the melt-spun ribbon, the thicknesses of the first two regions (I and II) were ∼18 and ∼3 μm, respectively. Moreover, the arm spacing measurements showed that the cellular structure was at least 10 times coarser in region III than the region closest to the chill side (region I). Correspondingly, the first two regions at the bottom of the ribbon were referred to as microcellular, while the region at the free surface was called coarse cellular.

The accuracy of our model in predicting the location of microstructure fineness alternation was confirmed by a comparison between the experimentally obtained microstructures of the rapidly solidifying Al-2Fe alloy and the interfacial velocity profiles obtained from MS and AM simulations. The locations of transition points also lined up with those observed in the interfacial temperature profiles depicted in Fig. 3. It was suggested that the initial undercooling or the onset of nucleation dictates the variations of growth rate (interface velocity) throughout the solidification process, and the growth rate in return decides the microstructure developed.

C. Development of fine microcellular microstructures

Microhardness measurements of annealed Al-Fe-V melt-spun ribbons revealed that fine microcellular ("featureless") regions maintain greater microhardness levels over the whole temperature range [20]. Depending on the application, increasing the proportion of the fine microcellular region within the rapidly solidified microstructure of melt-spun ribbon may be advantageous. Hence, a thorough understanding of the microstructural formation mechanisms is required for achieving desired properties in different applications. Nevertheless, the formation mechanism of the fine microcellular region is not fully understood because the controlling variables (interfacial velocity, temperature, and solute concentration) at the solid-liquid interface are not accessible. Here, the formation mechanism of the fine microcellular region will be revealed by thoroughly analyzing the evolutions of the controlling interface variables during the MS process. This subsection includes a comprehensive analysis based on the MS simulation presented in the previous subsection. First, looking at the Al-rich side of the Al-Fe system phase diagram, the solidification path of the MS process will be precisely described using the temperature and solute concentration values recorded at the interface. Next, the rapid solidification of the melt-spun ribbon will be further explored by tracing the variation of solute concentration in the liquid and solid phases as the solidification progresses.

To investigate the solidification path of MS, the evolution of temperature and solute concentration of the interface are plotted on top of the Al-Fe phase diagram. This phase diagram is constructed based on the free energies [66] used for

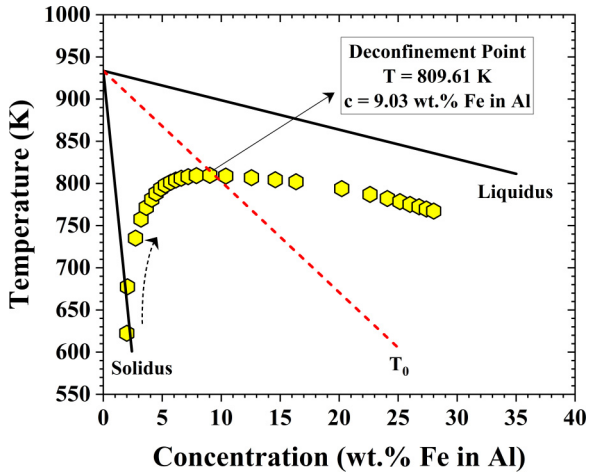

FIG. 6. The evolution of interfacial temperature and solute concentration plotted in the aluminum-rich side of the phase diagram for the Al-Fe system.

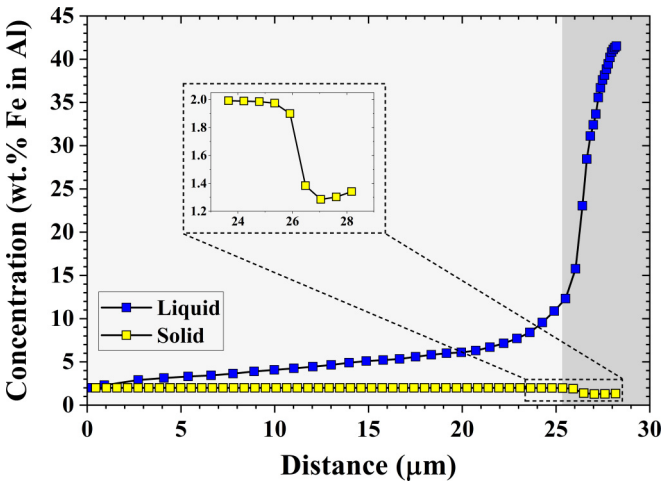

FIG. 7. The evolution of solute concentration on the solid and liquid sides of the interface as a function of distance from the chill side.

the phase-field model. As shown in Fig. 6, the solidification process in the melt-spun ribbon starts below the solidus line. It continues as the solute concentration and temperature values rise simultaneously until the solidification path intersects the T_0 line where the free energies of solid and liquid phases are identical. The intersection of the solidification path and the T_0 line is denoted as the *deconfinement point* since the complete solute trapping occurs only when the system is located below the T_0 line and becomes thermodynamically unfavorable when the solidification path crosses it and enters the right side of the two-phase region [67]. Noticeably, from this point on, the temperature profile displays a declining trend as the solute concentration further increases. Hence, it is natural to ask the following: (1) Does this deconfinement point correspond to the boundary of the fine microcellular region? (2) If it does, why does it happen at the T_0 line?

To further examine this idea, the corresponding locations of the deconfinement point in the interfacial velocity, temperature, and solute concentration profiles are identified in Figs. 3(a), 4(b), and 7, respectively. The deconfinement point corresponds to a variation in the temperature vs interface position plot. As shown in Fig. 3(a), the interfacial temperature gradually increases until it eventually reaches a maximum at the deconfinement point (∼25 μm away from the chill side), followed by a sharp decrease. In terms of interfacial velocity, the deconfinement point is identified to be at the same distance from the chill side. The transition between the low- and high-velocity regimes at the deconfinement point backs our prior thickness estimation of the fine microcellular region based on the MS velocity profile depicted in Fig. 4(b).

The solute concentration variations of the solid and liquid phases throughout the whole solidified melt-spun ribbon are plotted in Fig. 7 to illustrate the solute trapping effect across the ribbon. (The method to determine the solute concentration on the liquid side of the interface is detailed in the Supplemental Material [62].) It should be noted that the simulation results are for the evolution of the solidification front only. The solidification front can be regarded as the front tip of the solidifying dendrite or cell, which eventually becomes the center of the primary dendrites or cells. On the sides of the solidification front, the temperature may be higher due to thermal diffusion, the interfacial velocity may be slower, and solute segregation may happen. It was observed that the solute concentrations of both phases at the solidification front are the same as the nominal composition of the molten alloy at the beginning of solidification, but as the interface proceeds, the liquid concentration begins to gently increase while the solid concentration remains the same throughout most of the ribbon thickness. This is due to the decrease in interface velocity [Fig. 4(b)], which lessens the solute trapping effect. These tendencies continue until the deconfinement point is reached, after which the liquid concentration sharply rises while the solid side experiences a clear fall (inset of Fig. 7). The uniform solid concentration prior to the deconfinement point corresponds to the diffusionless solidification happening at the solidification front, where a segregation-free single-phase solid is produced with the same composition as the parent melt [68]. However, as the solidification progresses sideways, the interface velocity decreases leading to the formation of fine microcellular structures. Therefore, this region corresponds to the fine microcellular structure observed in MS. In summary, our phase-field simulations not only predicted the possible formation of the fine microcellular region in MS but also demonstrated how the controlling variables vary when the interface goes across the T_0 line (the deconfinement point). A key question that needs to be addressed is why those variables change sharply at the deconfinement point. In the following, we apply the thermodynamic analysis on rapid solidification and explain why this happens.

The schematic free-energy curves and the corresponding equilibrium phase diagram are shown in Fig. 8 to assist our discussion on the thermodynamics of the solidification process. The free energies of α-solid and liquid are identical only at C_0 where the two curves meet. The corresponding point on the T_0 curve is the deconfinement point at this temperature (T_1). At T_1, for a given liquid of composition C_1, the corresponding free energies of liquid, α-solid, and two-phase mixture are denoted as G^1_L, G^1_α, and $G^1_{\alpha+L}$, respectively. The

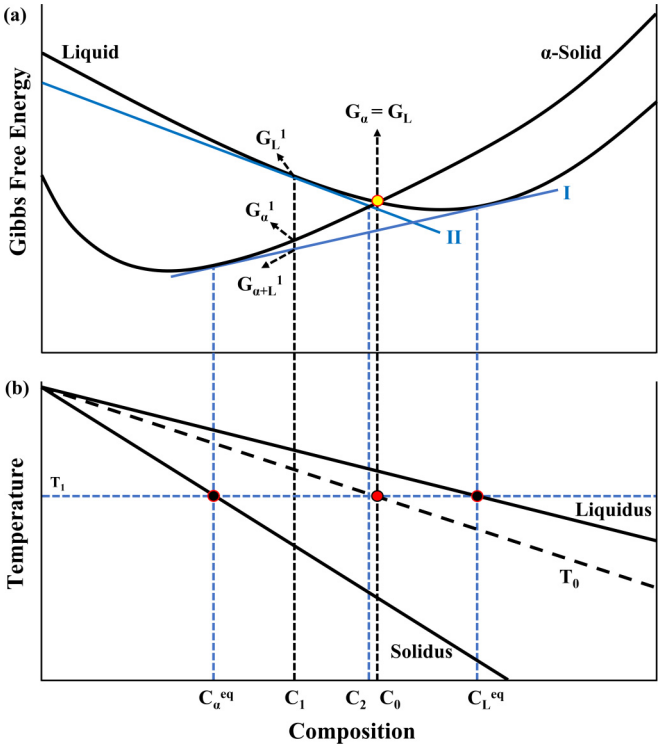

FIG. 8. (a) The free energy curves of α-solid and liquid. (b) The corresponding phase diagram.

possible range of α-solid compositions that may form from the initial liquid C_1 is restricted from 0 to C_2. Here, C_2 corresponds to the intersection of the α-solid free-energy curve and the tangent line II drawn at the starting composition C_1. The common tangent line I ensures the equilibrium of chemical potential. Here, C_α^{eq} and C_L^{eq} correspond to the compositions of equilibrium α-solid and liquid phases, respectively. In the composition range between C_α^{eq} and C_L^{eq}, the mixture of α-solid (of C_α^{eq}) and liquid (of C_L^{eq}) has the lowest total free energy. As a result, the nucleated α-solid undergoes an atomic rearrangement (referred to as local equilibrium) that alters its composition to one that allows it to coexist with a liquid of a different composition.

Given that G_L^1 is greater than G_α^1 and $G_{\alpha+L}^1$, the single-phase liquid is thermodynamically unstable and has a driving force for lowering its free energy to either G_α^1 or $G_{\alpha+L}^1$ depending on the solidification process. In the equilibrium conditions of a slow solidification where compositional changes occur, long diffusion times are needed for a two-phase mixture to emerge. The single phase α-solid (G_α^1) only forms in nonequilibrium processing conditions where the liquid is undercooled fast enough to alter its structure while maintaining the composition. Rapid solidification is an example of a nonequilibrium process in which the original liquid quickly transforms structurally into an α-solid of the same composition. This is so-called diffusionless solidification when the partitioning of solute atoms is not needed. Under equilibrium conditions, in contrast, the initial liquid converts to a two-phase mixture where partitioning is inevitable.

In the region where the composition is between C_0 and C_L^{eq}, the free energy of α-solid is always greater than that of liquid, which indicates that it is impossible to have diffusionless solidification. This region corresponds to the space between T_0 and liquidus on the phase diagram. Therefore, when the interface goes across the T_0 curve, diffusionless solidification is prohibited thermodynamically, while solute partitioning is required instead. Therefore, a sharp change in solute concentrations on both the solid and liquid sides of the interface is observed as shown in Fig. 7. Accordingly, the partition coefficient (ratio of solid concentration to liquid concentration) increases dramatically. Because solute partitioning is a much slower process than thermal diffusion, the interface velocity is limited by solute diffusion. In other words, the control mechanism of solidification growth switches from thermal- to solute-diffusion controlled when the interface gets to the deconfinement point (T_0 curve). The sharp velocity decrease causes a reduction in the release rate of latent heat. Consequently, the temperature of the interface begins to decrease.

Based on the preceding discussions, we concluded that the formation of the fine microcellular region in MS is due to the large initial undercooling that induces high interface velocities. The extraordinary driving force causes the phase transformation to happen so fast that there is not sufficient time for the system to fully explore all possible microscopic states in the phase space. As a result, the solidification proceeds with broken ergodicity as the local solidification happens faster than local structural and chemical changes and the solid appears from the liquid in a locally nonequilibrium condition. When the velocity of solid-liquid interface is equal or higher than the solute diffusion speed, the rapid solidification may go through a diffusionless (or chemically partitionless) transformation that could carry on over a range of driving forces [69,70]. Hence, the initial rapid solidification at the solidification front is diffusionless, and the interface is thermal diffusion controlled. As the interface crosses the T_0 line, the solute partitioning becomes thermodynamically required, the interface becomes solute diffusion controlled beyond this point, and its velocity drops abruptly. Eventually, this results in the formation of a relatively coarser microstructure. Therefore, the end of the fine microcellular region is where the interface touches the T_0 line (or the deconfinement point defined in this paper).

D. The role of nucleation and initial undercooling

The fine microcellular region was predicted in our simulations with at least semiquantitative accuracy, so the dependence of the thickness of this region on different conditions can be further explored here. These conditions can be classified into two subcategories: the processing variables and material properties. The initial undercooling and the nominal composition of the parent melt are found as the two most important factors in controlling the formation of fine microcellular regions.

First, we investigated the influence of undercooling on the thickness of the fine microcellular region by utilizing three different initial undercooling values, i.e., 373, 311, and 233 K. All the other material and simulation parameters are kept the same for these three simulations. Figures 9(a) and 9(b) depict the evolutions of growth velocity and temperature of the interface as functions of the distance from the chill side,

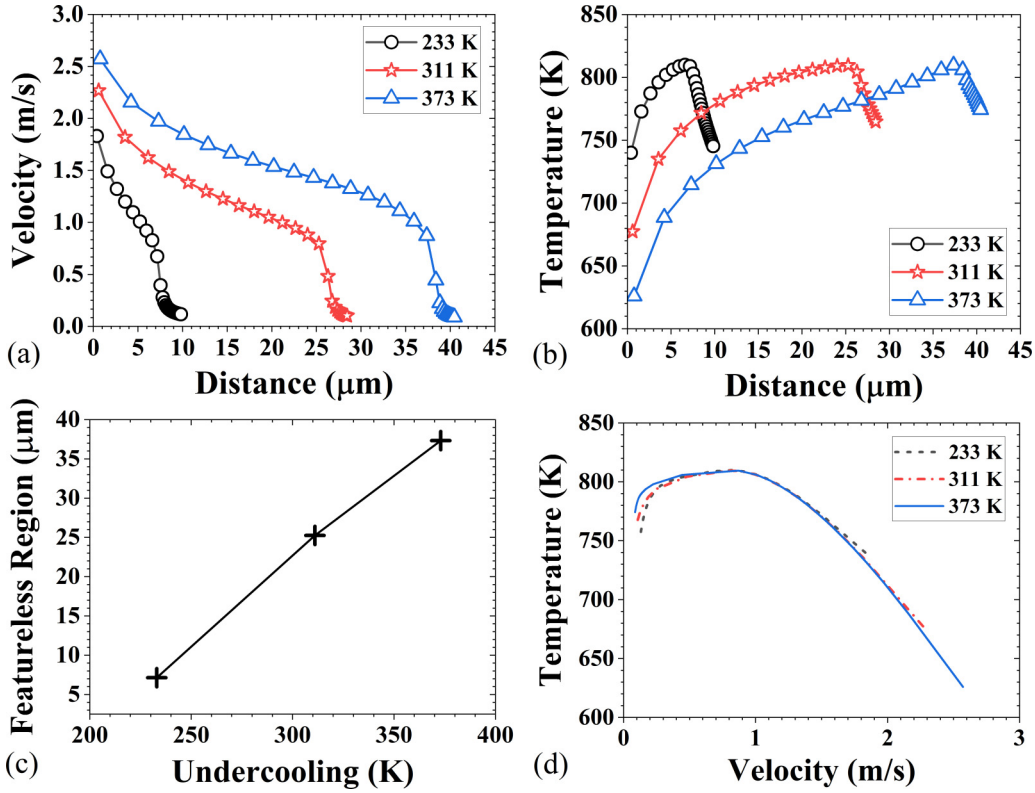

FIG. 9. (a) and (b) The interfacial growth velocity and temperature evolutions against the distance from the chill side, respectively. (c) The thickness of fine microcellular region vs undercooling. (d) Interfacial temperature vs velocity.

respectively. All three case studies showed similar patterns in velocity and temperature variations. The velocity profile has distinct low and high regimes with a narrow transition band, while the temperature is continuously increasing until it reaches the corresponding deconfinement point position where it drops abruptly. The highest temperature achieved in all cases is ~ 809 K, which is the same as the temperature recorded at the deconfinement point in Fig. 6. Based on the velocity profiles, the thickness of the fine microcellular regions is measured and denoted by W_1–W_3. The deconfinement point is assumed to be the location of the microstructural transition of fine to coarse. Moreover, as shown in Fig. 9(c), the measured thickness of the fine microcellular region increases linearly with the applied undercooling prior to nucleation. Lastly, the temperature vs velocity curves depicted in Fig. 9(d) show a very similar development path, except for a difference in the starting points. In conclusion, the thickness of the fine microcellular region formed from a melt of a given composition can be varied depending on the undercooling provided at the chill side. Therefore, the size of the fine microcellular region can be manipulated by changing the nucleation conditions. Inoculation may greatly reduce the nucleation barrier and leads to the formation of a thin fine microcellular region, while by purifying the melt (reducing the impurities) the fine microcellular region can be expanded.

E. The role of composition

Furthermore, the effect of the nominal composition on the formation of the fine microcellular region is discussed here. In this set of simulations, melts with nominal compositions of 2, 4, 6, and 8 wt. % Fe were subjected to a fixed undercooling of 311 K. In all four cases, the solidification was allowed to continue until the solidification front reached a distance of 30 μm from the chill side. Then according to the position of the deconfinement point in each case, the thickness of the fine microcellular region was measured. Eventually, the fraction of the fine microcellular region inside the melt-spun ribbon as a function of the nominal composition of the melt (Fe content) was plotted in Fig. 10.

The results showed a strong dependency of fine microcellular region fraction on the composition of the parent melt, e.g., the fraction of the fine microcellular region decreased from 46 to 32% when the composition of parent melt increased from 2 to 8 wt. % Fe. This dependency was previously noticed in the rapidly solidified melt-spun Al-Fe alloys [59], which is also plotted in Fig. 10 for comparison. Although the calculated fraction of fine microcellular region is higher than what was experimentally observed, especially for low-Fe alloys, our findings support the dependency of fraction of fine microcellular region on the Fe content. The observed disparity between simulation and experiment may be caused by the selection of the initial undercooling and the phase-field mobility M_ϕ. As both the real initial undercooling and interface velocity are not available from the experiments, we are unable to determine those two parameters for the phase-field simulation.

The results from this part have demonstrated that the nominal composition of the molten alloy has an impact on the microstructural development of the fine microcellular region. The composition of the matrix phase is closely related to the

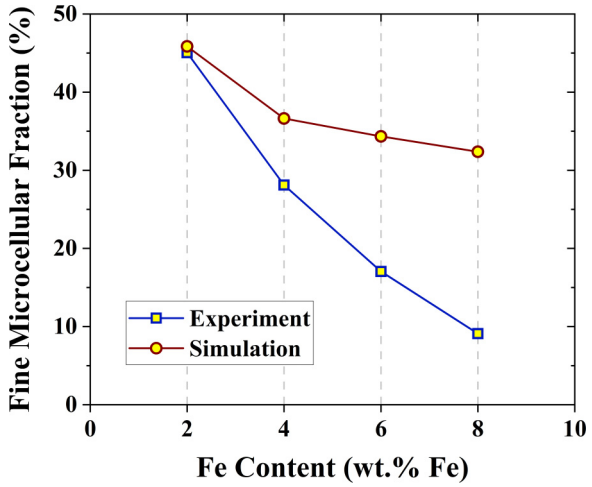

FIG. 10. Fraction of fine microcellular region (%) in melt-spun ribbon as a function of Fe content. The experimental data is taken from Chu and Granger [21].

solid solution strengthening and precipitation strengthening effect. Superhigh strength of the fine microcellular region may be achieved by manipulating the composition of the alloy and suppressing initial nucleation. In addition, the aging heat treatment of Al-Fe can introduce $Al_{13}Fe_4$ or Al_6Fe intermetallic phases, which show excellent stability at elevated temperatures. Therefore, the findings above provide an avenue for designing Al alloys for elevated temperature applications.

IV. CONCLUSIONS

In this paper, we investigated the microstructure development in two rapid solidification processes, AM and MS, using phase-field modeling. The phase-field model, which incorporated the coupled thermal-solute diffusion and solute trapping, enables direct access to all the key variables of the growth front (temperature, solute concentration, and velocity) for the entire rapid solidification process of both AM and MS. The variations of those variables show clear correlations with the observed microstructure features. By further thermodynamic and kinetic analysis, the underlying mechanism of microstructure development for AM and MS was revealed. The major findings can be summarized as follows:

The phase-field model can reproduce the structural transitions of coarse to fine (in AM) and fine to coarse (in MS) in the rapid solidification at least semiquantitatively. The calculated width of each zone/layer agrees well with experimental observations.

In AM, the solidification of the melt pool typically starts with an epitaxial growth which requires almost no undercooling and results in a relatively high initial interface temperature and a low initial velocity. In MS, by contrast, the absence of potent nucleation sites needs a considerable undercooling, which leads to a super high initial velocity and hence broken ergodicity. Consequently, the rapid release of latent heat increases the local temperature of the interface, resulting in coalescence.

Due to different initial interface temperatures and velocities, AM and MS select different solidification pathways. AM starts with a high temperature (liquidus), and the interface temperature keeps decreasing. In contrast, MS starts with a low temperature (below solidus), and the interface temperature keeps increasing until it reaches the T_0 line. Then the interface temperature decreases gently.

The formation of layers/zones is caused by the switching of the control mechanisms of solidification growth (or interface movement). In AM, the solidification front is initially controlled by solute diffusion and switches to thermal diffusion controlled when the interface temperature drops below solidus. In MS, it is the opposite. The solidification front is initially controlled by thermal diffusion and switches to solute diffusion controlled when the interface reaches the T_0 line on the phase diagram. The switching of the control mechanisms causes an abrupt velocity change, which leads to the observed coarse-to-fine and fine-to-coarse structural transitions in AM and MS, respectively.

The selection of different solidification pathways caused by the nucleation barrier provides a horizon for manipulating the microstructures in rapid solidification processes. By controlling the nucleation through inoculation or variation in alloy chemistry, the microstructure transition sequence, layer thickness, and phase selection can be manipulated. These findings can be directly used in laser repairing processes to achieve identical microstructures as the original component. They also provide guidelines for designing functionally graded alloys, as both similar and dissimilar solid phases may form during the AM build. In summary, in this paper, we unveiled the fundamentals of microstructure development during AM and MS, which set the foundations for building a processing-microstructure relationship in solidification processes.

ACKNOWLEDGMENT

This paper was supported in part by the National Science Foundation under Grant No. OAC-1919789. Saeid Alipour is thanked for helping with the schematic drawings.

The authors declare no competing financial interests.

[1] P. Duwez, R. H. Willens, and W. Klement Jr., Continuous series of metastable solid solutions in silver-copper alloys, J. Appl. Phys. **31**, 1136 (1960).

[2] W. Klement Jr., R. H. Willens, and P. O. L. Duwez, Noncrystalline structure in solidified gold–silicon alloys, Nature (London) **187**, 869 (1960).

[3] H. Jones, *Rapid solidification of metals and alloys* (The institution of metallurgists, London, UK, 1982).

[4] W. Kurz, B. Giovanola, and R. Trivedi, Theory of microstructural development during rapid solidification, Acta Metall. **34**, 823 (1986).

[5] S. Kou, *Welding Metallurgy* (John Wiley & Sons, Hoboken, 2003).

[6] C.-H. Hung, W.-T. Chen, M. H. Sehhat, and M. C. Leu, The effect of laser welding modes on mechanical properties and microstructure of 304L stainless steel parts fabricated by

laser-foil-printing additive manufacturing, Int. J. Adv. Manuf. Technol. **112**, 867 (2021).

[7] P. Mohammadpour, A. Plotkowski, and A. B. Phillion, Revisiting solidification microstructure selection maps in the frame of additive manufacturing, Addit. Manuf. **31**, 100936 (2020).

[8] M. H. Sehhat, A. Mahdianikhotbesara, and F. Yadegari, Impact of temperature and material variation on mechanical properties of parts fabricated with fused deposition modeling (FDM) additive manufacturing, Int. J. Adv. Manuf. Technol. **120**, 4791 (2022).

[9] K. Sisco, A. Plotkowski, Y. Yang, D. Leonard, B. Stump, P. Nandwana, R. R. Dehoff, and S. S. Babu, Microstructure and properties of additively manufactured Al–Ce–Mg alloys, Sci. Rep. **11**, 6953 (2021).

[10] A. Plotkowski, O. Rios, N. Sridharan, Z. Sims, K. Unocic, R. T. Ott, R. R. Dehoff, and S. S. Babu, Evaluation of an Al-Ce alloy for laser additive manufacturing, Acta Mater. **126**, 507 (2017).

[11] G. P. Dinda, A. K. Dasgupta, and J. Mazumder, Evolution of microstructure in laser deposited Al–11.28% Si alloy, Surf. Coat. Technol. **206**, 2152 (2012).

[12] J. R. Croteau, S. Griffiths, M. D. Rossell, C. Leinenbach, C. Kenel, V. Jansen, D. N. Seidman, D. C. Dunand, and N. Q. Vo, Microstructure and mechanical properties of Al-Mg-Zr alloys processed by selective laser melting, Acta Mater. **153**, 35 (2018).

[13] H. Zhang, H. Zhu, X. Nie, J. Yin, Z. Hu, and X. Zeng, Effect of zirconium addition on crack, microstructure and mechanical behavior of selective laser melted Al-Cu-Mg alloy, Scr. Mater. **134**, 6 (2017).

[14] A. B. Spierings, K. Dawson, K. Kern, F. Palm, and K. Wegener, SLM-processed Sc-and Zr-modified Al-Mg alloy: Mechanical properties and microstructural effects of heat treatment, Mater. Sci. and Eng.: A **701**, 264 (2017).

[15] A. B. Spierings, K. Dawson, T. Heeling, P. J. Uggowitzer, R. Schäublin, F. Palm, and K. Wegener, Microstructural features of Sc-and Zr-modified Al-Mg alloys processed by selective laser melting, Mater. Des. **115**, 52 (2017).

[16] A. B. Spierings, K. Dawson, M. Voegtlin, F. Palm, and P. J. Uggowitzer, Microstructure and mechanical properties of as-processed scandium-modified aluminium using selective laser melting, CIRP Ann. **65**, 213 (2016).

[17] R. Li, M. Wang, Z. Li, P. Cao, T. Yuan, and H. Zhu, Developing a high-strength Al-Mg-Si-Sc-Zr alloy for selective laser melting: Crack-inhibiting and multiple strengthening mechanisms, Acta Mater. **193**, 83 (2020).

[18] J. H. Martin, B. D. Yahata, J. M. Hundley, J. A. Mayer, T. A. Schaedler, and T. M. Pollock, 3D printing of high-strength aluminium alloys, Nature (London) **549**, 365 (2017).

[19] X. Qi, N. Takata, A. Suzuki, M. Kobashi, and M. Kato, Laser powder bed fusion of a near-eutectic Al–Fe binary alloy: Processing and microstructure, Addit. Manuf. **35**, 101308 (2020).

[20] D. J. Skinner and K. Okazaki, High strength Al-Fe-V alloys at elevated temperatures produced by rapid quenching from the melt, Scr. Metall. **18**, 905 (1984).

[21] M. G. Chu and D. A. Granger, Solidification and microstructure analysis of rapidly solidified melt-spun Al-Fe alloys, Metall. Trans. A **21**, 205 (1990).

[22] R. Mehrabian, Rapid Solidification, Int. Mater. Rev. **27**, 185 (1982).

[23] W. Kurz and R. Trivedi, Rapid solidification processing and microstructure formation, Mater. Sci. Eng.: A **179**, 46 (1994).

[24] C. Zhao, K. Fezzaa, R. W. Cunningham, H. Wen, F. de Carlo, L. Chen, A. D. Rollett, and T. Sun, Real-time monitoring of laser powder bed fusion process using high-speed x-ray imaging and diffraction, Sci. Rep. **7**, 3602 (2017).

[25] J. T. McKeown, A. J. Clarke, and J. M. K. Wiezorek, Imaging transient solidification behavior, MRS Bull. **45**, 916 (2020).

[26] J. T. McKeown, A. K. Kulovits, C. Liu, K. Zweiacker, B. W. Reed, T. LaGrange, J. M. K. Wiezorek, and G. H. Campbell, *In situ* transmission electron microscopy of crystal growth-mode transitions during rapid solidification of a hypoeutectic Al–Cu Alloy, Acta Mater. **65**, 56 (2014).

[27] V. Bathula, C. Liu, K. Zweiacker, J. McKeown, and J. M. K. Wiezorek, Interface velocity dependent solute trapping and phase selection during rapid solidification of laser melted hypoeutectic Al-11 at. % Cu alloy, Acta Mater. **195**, 341 (2020).

[28] J. D. Roehling, D. R. Coughlin, J. W. Gibbs, J. K. Baldwin, J. C. E. Mertens, G. H. Campbell, A. J. Clarke, and J. T. McKeown, Rapid solidification growth mode transitions in Al-Si alloys by dynamic transmission electron microscopy, Acta Mater. **131**, 22 (2017).

[29] P. Gilgien, A. Zryd, and W. Kurz, Metastable phase diagrams and rapid solidification processing, ISIJ Int. **35**, 566 (1995).

[30] W. Kurz and D. J. Fisher, *Fundamentals of Solidification* (Trans Tech Publications Ltd., Uetikon-Zurich, 1998).

[31] M. Zimmermann, M. Carrard, and W. Kurz, Rapid solidification of Al-Cu eutectic alloy by laser remelting, Acta Metall. **37**, 3305 (1989).

[32] S. C. Gill and W. Kurz, Rapidly solidified Al-Cu alloys—II. Calculation of the microstructure selection map, Acta Metall. Mater. **43**, 139 (1995).

[33] S. C. Gill, M. Zimmermann, and W. Kurz, Laser resolidification of the $AlAl_2Cu$ eutectic: The coupled zone, Acta Metall. Mater. **40**, 2895 (1992).

[34] M. Zimmermann, M. Carrard, M. Gremaud, and W. Kurz, Characterization of the banded structure in rapidly solidified Al-Cu alloys, Mater. Sci. Eng.: A **134**, 1278 (1991).

[35] J. Lipton, W. Kurz, and R. Trivedi, Rapid dendrite growth in undercooled alloys, Acta Metall. **35**, 957 (1987).

[36] S. Fukumoto and W. Kurz, Solidification phase and microstructure selection maps for Fe-Cr-Ni Alloys, ISIJ Int. **39**, 1270 (1999).

[37] W. J. Boettinger, J. A. Warren, C. Beckermann, and A. Karma, Phase-field simulation of solidification, Annu. Rev. Mater. Res. **32**, 163 (2002).

[38] L.-Q. Chen, Phase-field models for microstructure evolution, Annu. Rev. Mater. Res. **32**, 113 (2002).

[39] N. Moelans, B. Blanpain, and P. Wollants, An introduction to phase-field modeling of microstructure evolution, Calphad **32**, 268 (2008).

[40] A. A. Wheeler, W. J. Boettinger, and G. B. McFadden, Phase-field model of solute trapping during solidification, Phys. Rev. E **47**, 1893 (1993).

[41] I. Steinbach, L. Zhang, and M. Plapp, Phase-field model with finite interface dissipation, Acta. Mater. **60**, 2689 (2012).

[42] P. K. Galenko, E. V. Abramova, D. Jou, D. A. Danilov, V. G. Lebedev, and D. M. Herlach, Solute trapping in rapid

solidification of a binary dilute system: A phase-field study, Phys. Rev. E **84**, 041143 (2011).
[43] D. Danilov and B. Nestler, Phase-field modelling of nonequilibrium partitioning during rapid solidification in a non-dilute binary alloy, Discrete Contin. Dyn. Syst. **15**, 1035 (2006).
[44] J. Kundin, L. Mushongera, and H. Emmerich, Phase-field modeling of microstructure formation during rapid solidification in Inconel 718 superalloy, Acta Mater. **95**, 343 (2015).
[45] T. Pinomaa and N. Provatas, Quantitative phase field modeling of solute trapping and continuous growth kinetics in quasi-rapid solidification, Acta Mater. **168**, 167 (2019).
[46] H. Wang, F. Liu, G. J. Ehlen, and D. M. Herlach, Application of the maximal entropy production principle to rapid solidification: A multi-phase-field model, Acta Mater. **61**, 2617 (2013).
[47] D. Danilov and B. Nestler, Phase-field modelling of solute trapping during rapid solidification of a Si–As alloy, Acta Mater. **54**, 4659 (2006).
[48] L. Zhang, E. V. Danilova, I. Steinbach, D. Medvedev, and P. K. Galenko, Diffuse-interface modeling of solute trapping in rapid solidification: Predictions of the hyperbolic phase-field model and parabolic model with finite interface dissipation, Acta Mater. **61**, 4155 (2013).
[49] M. Conti, Thermal and chemical diffusion in the rapid solidification of binary alloys, Phys. Rev. E **61**, 642 (2000).
[50] M. Conti, Heat diffusion and banding in rapid solidification, Phys. Rev. E **58**, 6166 (1998).
[51] R. Acharya, J. A. Sharon, and A. Staroselsky, Prediction of microstructure in laser powder bed fusion process, Acta Mater. **124**, 360 (2017).
[52] D. Liu and Y. Wang, Mesoscale multi-physics simulation of rapid solidification of Ti-6Al-4V alloy, Addit. Manuf. **25**, 551 (2019).
[53] A. Karma, Phase-Field Formulation for Quantitative Modeling of Alloy Solidification, Phys. Rev. Lett. **87**, 115701 (2001).
[54] Y. Gu, X. He, and D. Han, On the phase-field modeling of rapid solidification, Comput. Mater. Sci. **199**, 110812 (2021).
[55] S. G. Kim, W. T. Kim, and T. Suzuki, Phase-field model for binary alloys, Phys. Rev. E **60**, 7186 (1999).
[56] J. T. McKeown, K. Zweiacker, C. Liu, D. R. Coughlin, A. J. Clarke, J. K. Baldwin, J. W. Gibbs, J. D. Roehling, S. D. Imhoff, and P. J. Gibbs, Time-resolved in situ measurements during rapid alloy solidification: Experimental insight for additive manufacturing, JOM **68**, 985 (2016).
[57] K. W. Zweiacker, C. Liu, M. A. Gordillo, J. T. McKeown, G. H. Campbell, and J. M. K. Wiezorek, Composition and automated crystal orientation mapping of rapid solidification products in hypoeutectic Al-4 at.% Cu alloys, Acta Mater. **145**, 71 (2018).
[58] T. W. Clyne, Numerical treatment of rapid solidification, Metall. Trans. B **15**, 369 (1984).
[59] M. G. Chu, A. Giron, and D. A. Granger, Microstructure and heat flow in melt-spun aluminum alloys, in *Proc. Int. Conf. on Rapidly Solidified Materials*, 3 (ASM International, Materials Park, 1986).
[60] J. J. Valencia and K.-O. Yu, Thermophysical properties, in *Modeling for Casting and Solidification Processing*, edited by K.-O. Yu (Marcel Dekker, Inc., New York, 2013), Chap. 6, p. 189.
[61] A. L. Greer, A. M. Bunn, A. Tronche, P. v Evans, and D. J. Bristow, Modelling of inoculation of metallic melts: Application to grain refinement of aluminium by Al–Ti–B, Acta Mater. **48**, 2823 (2000).
[62] See Supplemental Material at http://link.aps.org/supplemental/10.1103/PhysRevMaterials.7.023403 for the analysis of nucleation and determination of solute concentration.
[63] Y. Gu and L. Chen, Switching of controlling mechanisms during the rapid solidification of a melt pool in additive manufacturing, arXiv:2208.01487 (2022).
[64] D. Bouchard and J. S. Kirkaldy, Prediction of dendrite arm spacings in unsteady-and steady-state heat flow of unidirectionally solidified binary alloys, Metall. Mater. Trans. B **28**, 651 (1997).
[65] M. C. Flemings, Solidification processing, Metall. Mater. Trans. B **5**, 2121 (1974).
[66] B. Echebarria, R. Folch, A. Karma, and M. Plapp, Quantitative phase-field model of alloy solidification, Phys. Rev. E **70**, 061604 (2004).
[67] J. C. Baker and J. W. Cahn, Thermodynamics of solidification, in *The Selected Works of John W. Cahn*, edited by W. C. Carter and W. C. Johnson (John Wiley & Sons, Ltd, Hoboken, 1998), Chap. 26, pp. 253–288.
[68] H. Biloni and B. Chalmers, Predendritic solidification, Trans. Metall. Soc. AIME **233**, 373 (1965).
[69] P. K. Galenko and D. Jou, Rapid solidification as non-ergodic phenomenon, Phys. Rep. **818**, 1 (2019).
[70] P. K. Galenko, V. Ankudinov, K. Reuther, M. Rettenmayr, A. Salhoumi, and E. V. Kharanzhevskiy, Thermodynamics of rapid solidification and crystal growth kinetics in glass-forming alloys, Philos. Trans. R. Soc. A **377**, 20180205 (2019).